Electronic Supplementary Information

Passive Droplet Sorting using Viscoelastic Flow Focusing

Andrew C. Hatch,[a] Apurva Patel,[a] N. Reginald Beer,[b] and Abraham P. Lee*[a]

I. Supplemental Theory

Work by Leal (1979) described lateral migration of spherical drops when one or both fluids are viscoelastic and modeled as a second order fluid[1]. These findings also demonstrate that lateral droplet migration is highly dependent on the ratio of internal and external viscosities, κ, and the ratio of internal and external fluid Weissenberg numbers, δ=Wii/Wio, but that the rate of droplet migration was rather insensitive to which fluid was viscoelastic. For large κ-values, the droplets act like rigid spheres and deformation becomes small. In this case, wall repulsion forces dominate and force the droplet or rigid particle toward the centerline of the flow profile, independent of whether the shear rate increases or decreases in this direction[2].

However, it must be emphasized that the experimental and theoretical findings of Chan and Leal (1979) were limited to the case where the ratio of droplet diameter to plane wall spacing, $\zeta = a/d$, droplet deformation, and non-dimensional Reynolds, Re, and Capillary, Ca, numbers were all small, but the droplet spacing, $s=y/d$, was large. The non-dimensional Capillary, Reynolds, Weissenberg, Elasticity, and Dean numbers are described in equations S1-S5. For square and rectangular channels, the mean hydraulic diameter, D_H, is used as the characteristic length term in the non-dimensionalized equations defined as $D_H = 4A/P = 2hw/(h+w)$.

Capillary number

$$Ca = \frac{\mu V}{\gamma} = \frac{\mu Q_o}{\gamma hw} \tag{S1}$$

Reynolds number in rectangular channel:

$$Re = \frac{\rho V D_H}{\mu} \tag{S2}$$

Weissenberg number in rectangular channel [3,4]:

$$Wi = \dot{\gamma}\lambda = \frac{2Q_o}{hw^2}\lambda \tag{S3}$$

Elasticity number in rectangular channel:

$$El = \frac{Wi}{Re} = \frac{\lambda\mu(w+h)}{\rho hw^2} \tag{S4}$$

Dean number for curved channels:

$$De = \frac{\rho V D_H}{\mu}\left(\frac{D_H}{2R}\right)^{1/2} \tag{S5}$$

In these equations μ is the dynamic (absolute) fluid viscosity, ρ is the fluid density, γ is the interfacial tension between the inner and outer fluid phase, λ is the relaxation rate of the viscoelastic fluid, and R is the radius of curvature of the channel. The shear rate, $\dot{\gamma}$, of a fluid in a rectangular channel is defined as $\dot{\gamma} = \sim(6Q_o)/(wh^2)$ where h is the smaller of the two channel cross-sections [5].

One difficulty in working with a two-phase fluid flow profile is that the characteristic behavior of the outer and inner fluid phase is much more difficult to solve compared to single-phase fluid flow, which can be easily estimated using standard numerical methods. Several analytical and experimental works have been published to investigate droplet and capsule deformation and migration between planar walls and in tubes, however many do not investigate the internal viscoelastic forces which might exist [6–14]. Based on these findings, the actual shear rates and geometric shape of the inner droplet fluid phase can vary dramatically as a function of droplet position relative to bounding walls, droplet size relative to channel dimensions, viscosity ratio of inner and outer fluid phase, and the degree of droplet deformation. An example of internal droplet fluid velocities relative to the surrounding oil phase in a tube flow has been calculated by Coulliette et al. (1997)[10].

What is not clear from prior work is how the viscosity ratio of the two fluid phases varies depending on the viscoelastic polymer contribution to the viscosity and the shear rates transferred from the outer fluid phase to the inner fluid phase. Furthermore, the local recirculating flows of both fluid phases in the immediate vicinity of the droplets cause an even greater degree of uncertainty. A more complete theoretical analysis of the underlying physics describing a viscoelastic two-phase fluid system is required to achieve a greater understanding of the droplet migration behavior. Short of the ability to model this behavior, it was found useful to describe the fluid phases as Newtonian, or weakly and strongly non-Newtonian, and to describe the viscosity ratio in terms of their infinite-shear viscosity. This simplification seemed appropriate for the reason that the fluids utilized in these experiments were all found to be very near Newtonian based on rheometer measurements.

II. Supplemental Sorting Designs and Considerations

To achieve passive viscoelastic droplet sorting, several different channel designs were conceived to best enhance droplet migration behavior over the length of the channel, several of which are illustrated in Figures S1 & S2. Necessary design parameters included adequate channel length to allow sufficient droplet migration for equilibrium to be reached and separation to occur. As seen in the main text Figure 2 b), these lengths could easily exceed 5 cm lengths if droplets are small or weakly viscoelastic. For purposes of fabrication, overall design dimensions were limited to a 3" or 76 mm round silicon wafer and a 2" x 3" glass slide. In order to achieve longer channel lengths and accommodate more than a single design on a wafer, curved channels were utilized to obtain lengths ranging from 1.7-20 cm long, while straight channels were used to create lengths ranging from 0.5-5 cm long.

With the addition of curvature in the channels, a slight Deans flow effect is introduced into the cross sectional flow that can shift the equilibrium positions of the droplets within the channel[15]. It is expected that the contribution of Dean's flow, combined with the buoyancy of the droplet in the flourinert oil, will slightly shift the equilibrium positions of droplets away from their predicted locations because they are not accounted for in the theoretical predictions. In addition, the mere presence of droplets within the channels results in feedback to the flow profile and overall flow resistance which may result in flow instabilities and dynamic localized flow profiles[8,16]. The combination of these effects create relatively unpredictable migration behavior when multiple droplets are flowing in close proximity to each other, especially when considering various sizes will have varying feedback contributions to the localized flow profile.

Evidence of these unpredictable flow conditions are observed in the form of droplets hopping from one side-channel to another due to non-uniform resistance to flow profiles, and droplet leap-frogging where a droplet from behind may come around a droplet in front of it, consequently disturbing their migration positions within the channel. As not all of these effects are accounted for in the theory or experimental results, it is difficult to determine their overall contribution to the observed results. There was a certain degree of A-symmetry observed in the droplet migration equilibrium positions, seen in Figure 3 c) of the main text and Figure S4 below, and we mostly attribute this A-symmetry to these unknown effects.

Pinched flow designs have been demonstrated in prior works[17,18] for size based hydrodynamic sorting to exploit the higher shear gradients near the walls as seen in Figure S2 b). Theoretical migration shown in the main text Figure 2 c) illustrates how different injection locations of droplets causes them to separate faster when starting near the wall as opposed to the centerline of the channel. Different droplet migration rates were theoretically calculated for a range of droplet sizes and channel dimensions, with several key findings summarized in the main text Figure 2.

Based on the varying migration rates arising from subtle differences in droplet viscosity, it is conceivable that a monodisperse size distribution of viscoelastic droplets with a polydisperse viscosity distribution may utilize a pinched flow like sorting technique to isolate certain ranges of droplet viscosities. This effect would be amplified by the non-linear migration rates observed in the α-coefficient resulting in broad range of migration positions at the end of a shortened channel. In this work we focus more on the robust nature of positive and negative migration rates to result in different droplet equilibrium positions. This provides a lower dependence on droplet size and best exploits the viscoelastic behavior characteristics to achieve high enrichment factors and high throughputs.

Droplet enrichment factors were calculated based on the relative ratio of positive to negative migration droplets at the inlet compared to the same ratios at their respective outlets. Typical droplet generation frequencies for each droplet inlet ranged from 30-250 drops/sec and their relative ratios in frequency varied from 1:15 to 15:1. Two droplet fluid streams were merged together as shown in Video S1 then sent to the common droplet injection point for sorting as shown in Video S2.

Droplet dimensions of 30-100 μm where chosen to represent typical sizes used in droplet microfluidic applications and channel designs were developed to accommodate hydrodynamic based sorting of droplets on that scale. This resulted in a channel height of at least the largest droplet diameter, or ~100 μm, and a width of 2-5 times the largest droplet diameter, or ~200-500 μm. In addition, large droplet separations were desired at the end of the channel, requiring wide channels at the outlet, but rapid migrations were desired at the beginning of the channel, requiring narrow channels with higher shear gradients as illustrated in the main text Figure S2. In order to accomplish both, a gradually widening channel dimension was chosen to increase separation rates at the inlet and allow for greater migration separation at the outlet.
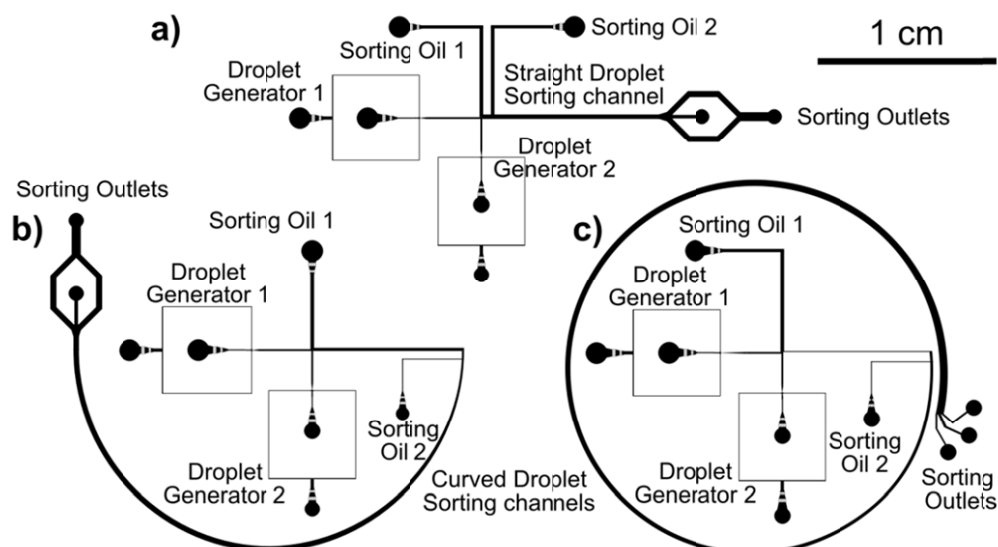
Supporting Figures:

Figure S1: Droplet sorting channels were designed with a variety of profiles to achieve useful droplet sorting. Curved channel designs were the primary mask/mold designs used for experimentation. a) straight channel with 1 cm length and 200 μm width. b) semi-circle and c) full-circle spiral channels with radius of curvature R ≈ 1.08 cm that correlates to a length of L≈1.7 cm per 90° rotation. Channels begin with a 100 μm channel width that gradually widens at a rate of ~50 μm/cm length resulting in 270 μm and 450 μm outlets respectively.
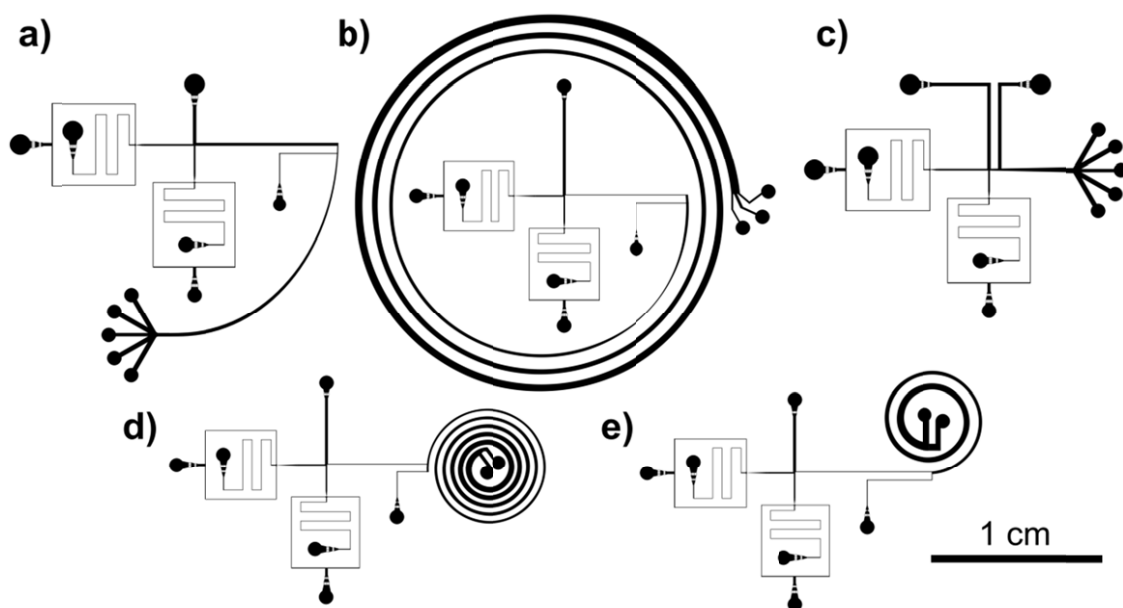

Figure S2: A variety of other channel designs were tested during these experiments to test variations in channel length, width, curvature, and gradually changing widths. a) Quarter circle design with 1.7 cm length and 180 μm outlet. b) Full circle design with 20 cm length ranging from 100 μm width at inlet to 500 μm width at outlet with an increase in width of 20 μm/cm. c) straight channel with 0.5 cm length, ranging from 100 μm at inlet to 300 μm at outlet. d) Small spiral channel with five turns having radius of curvatures of 3.5 mm at the widest to 1 mm at the center in 0.5 mm increments and channel widths ranging from 100 μm at the inlet to 350 μm at the outlet with a total length of ~8 cm. e) Small spiral channel with two turns having radius of curvatures of 3 mm at the widest to 1.5 mm at the center and channel widths ranging from 150 μm at the inlet to 500 μm at the outlet with a total length of ~3 cm.
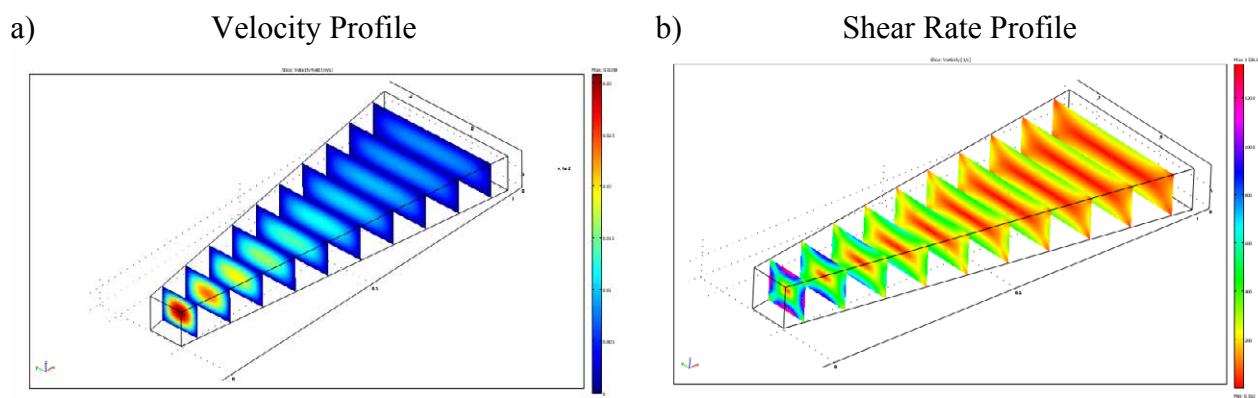
a) Velocity Profile b) Shear Rate Profile

Figure S3: a) Velocity and b) shear rate profiles within a microfluidic channel at gradually increasing h/w aspect ratios from 1:1 to 1:4. In small channels the shear stress ranges from zero at the channel center to $\dot{\gamma}_{max}$ at the middle of the top/bottom and left/right channel walls. Q_o=10 μL/min, h=100 μm, w=100 μm to 400 μm with corresponding $\dot{\gamma}_{max}$ of 1,336 s^{-1} to 400 s^{-1} for the narrow and wide channel widths respectively. It can be seen that in square and rectangular channel configurations, several local minima and maxima shear rate regions exist, each of which are potential resting/equilibrium positions for droplets tending to migrate toward high or low shear gradient positions. Predictive behavior from inertial microfluidics suggests that depending on the aspect ratio, droplets will be more likely to go to either 1) the sides of the channel, or 2) the top and bottom of the channel, caused by higher shear gradient profiles and lower distance paths of the varying geometries. However, droplets starting near the edge in a pinched flow design along with larger droplet diameters relative to channel height tend to disfavor their equilibrium positions from the top and bottom channel walls.
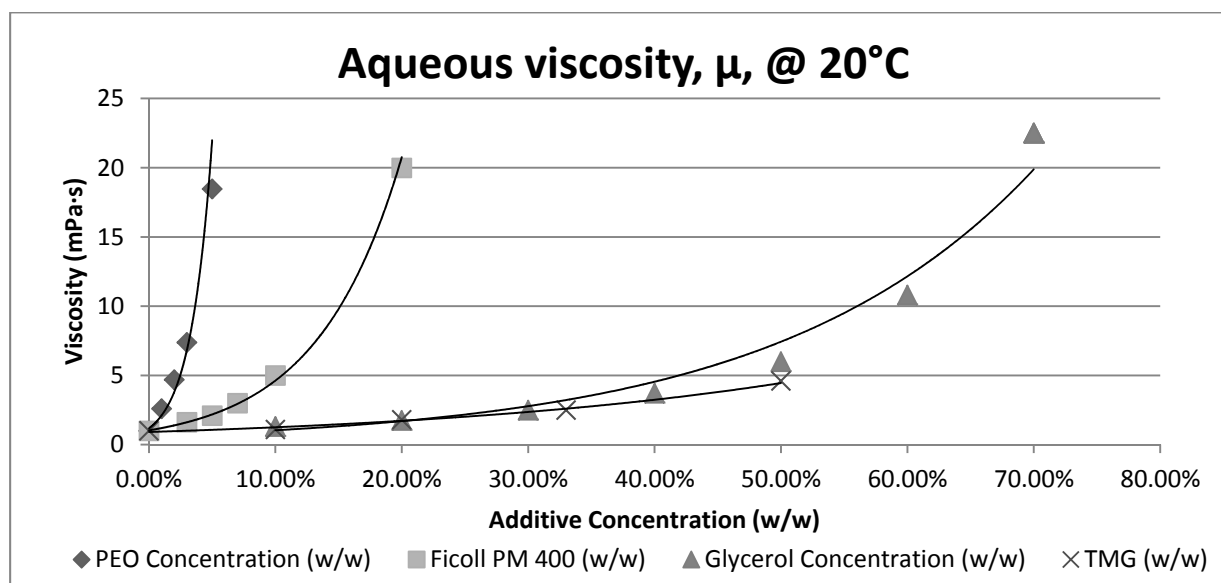

Figure S4: Infinite shear viscosities, μ_∞, of aqueous solutions are plotted as a function of concentration of viscosity modifying additives. In the rheometer experiments, there was no detectable viscoelastic behavior to characterize.
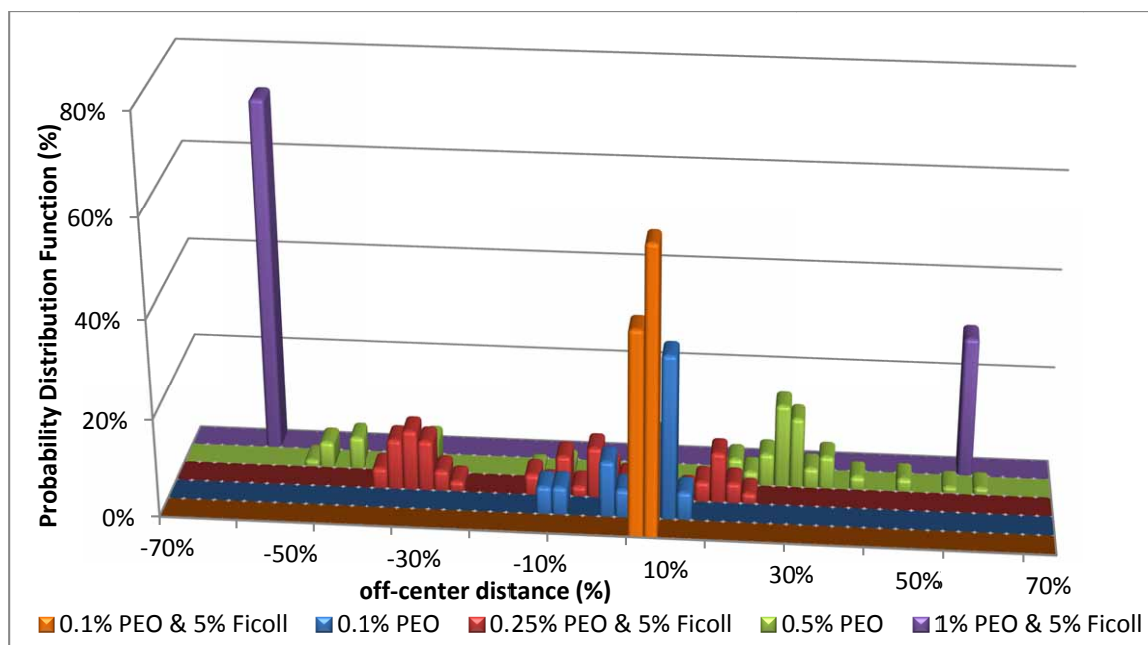
Figure S5: Probability distribution function of droplet equilibrium position as a function of polymer concentration and flow rate. Channel dimension: 180 μm wide x 100 μm height; flow rate: 20-30 μl/min; droplet diameter: ~75 μm; a/d ~ 0.4-0.5; Ca=0.008 and Re=0.8. The A-symmetry in droplet migration positions is attributed to several factors including the contribution of Dean's flow forces, droplet buoyancy, and flow feedback/instability from the presence of droplets themselves. Results are based on 500 frames of droplets streaming past the observation area captured at 125 or 250 frames/sec depending on flow rate. This resulted in a typical range of 30-60 droplets for each data set.
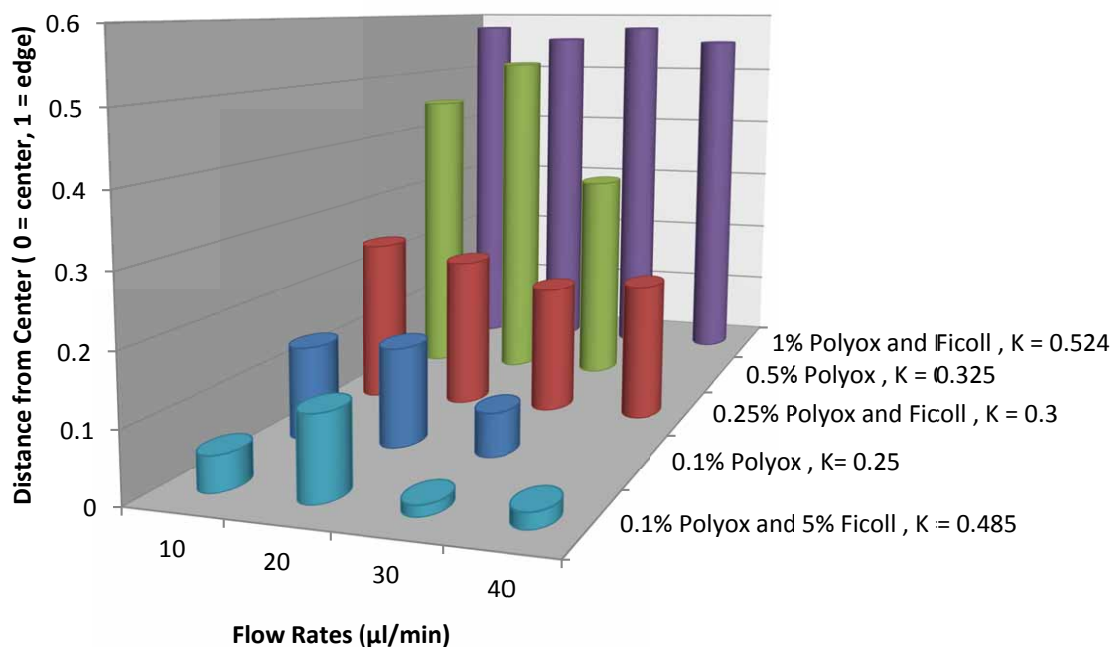

Figure S6: Mean droplet position as a function of polymer concentration and flow rate. Channel dimension: 180 μm wide x 100 μm height; flow rate: 20-30 μl/min; droplet diameter: ~75 μm; a/d ~ 0.4-0.5; Ca=0.008 and Re=0.8.

References:

1. L. G. Leal, *Journal of Non-Newtonian Fluid Mechanics*, 1979, **5**, 33–78.
2. J.-P. Matas, J. F. Morris, and éLisabeth Guazzelli, *Journal of Fluid Mechanics*, 2004, **515**, 171–195.
3. L. E. Rodd, T. P. Scott, D. V. Boger, J. J. Cooper-White, and G. H. McKinley, *Journal of Non-Newtonian Fluid Mechanics*, 2005, **129**, 1–22.
4. L. E. Rodd, J. J. Cooper-White, D. V. Boger, and G. H. McKinley, *Journal of Non-Newtonian Fluid Mechanics*, 2007, **143**, 170–191.
5. Y. Son, *Polymer*, 2007, **48**, 632–637.
6. P. C.-H. Chan and L. G. Leal, *International Journal of Multiphase Flow*, 1981, **7**, 83–99.
7. W. S. J. Uijttewaal, E.-J. Nijhof, and R. M. Heethaar, *Phys. Fluids A*, 1993, **5**, 819–825.
8. K. Feigl, D. Megias-Alguacil, P. Fischer, and E. J. Windhab, *Chemical Engineering Science*, 2007, **62**, 3242–3258.
9. W. Li, G. H. Ko, and D. Gersappe, *Physical Review E - Statistical, Nonlinear, and Soft Matter Physics*, 2005, **72**, 066305.
10. C. Coulliette and C. Pozrikidis, *Journal of Fluid Mechanics*, 1998, **358**, 1–28 M3 – null.
11. S. K. Doddi and P. Bagchi, *International Journal of Multiphase Flow*, 2008, **34**, 966–986.
12. J. R. Smart and J. Leighton, *Phys. Fluids A*, 1991, **3**, 21–28.
13. A. J. Griggs, A. Z. Zinchenko, and R. H. Davis, *International Journal of Multiphase Flow*, 2007, **33**, 182–206.
14. J. MAGNAUDET, S. TAKAGI, and D. LEGENDRE, *Journal of Fluid Mechanics*, 2003, **476**, 115–157.
15. S. S. Kuntaegowdanahalli, A. A. S. Bhagat, G. Kumar, and I. Papautsky, *Lab Chip*, 2009, **9**, 2973–2980.
16. V. Cristini and Y. C. Tan, *Lab Chip*, 2004, **4**, 257–264.
17. M. Chabert and J.-L. Viovy, *Proc. Natl. Acad. Sci. U. S. A.*, 2008, **105**, 3191–3196.
18. C.-H. Yang, Y.-S. Lin, K.-S. Huang, Y.-C. Huang, E.-C. Wang, J.-Y. Jhong, and C.-Y. Kuo, *Lab Chip*, 2009, **9**, 145–150.